Monthly Notices
of the
ROYAL ASTRONOMICAL SOCIETY

MNRAS **467,** 1222–1230 (2017)
Advance Access publication 2017 January 22

doi:10.1093/mnras/stx156

The AT-LESS CO(1–0) survey of submillimetre galaxies in the Extended *Chandra* Deep Field South: first results on cold molecular gas in galaxies at $z \sim 2$

Minh T. Huynh,[1,2★] B. H. C. Emonts,[3] A. E. Kimball,[4,5] N. Seymour,[6] Ian Smail,[7] A. M. Swinbank,[7] W. N. Brandt,[8,9,10] C. M. Casey,[11] S. C. Chapman,[12] H. Dannerbauer,[13,14,15] J. A. Hodge,[16] R. J. Ivison,[17,18] E. Schinnerer,[19] A. P. Thomson,[7] P. van der Werf[16] and J. L. Wardlow[7]

Affiliations are listed at the end of the paper

Accepted 2017 January 17. Received 2017 January 11; in original form 2016 September 30

ABSTRACT

We present the first results from our ongoing Australia Telescope Compact Array survey of ^{12}CO(1–0) in Atacama Large Millimeter Array (ALMA)-identified submillimetre galaxies (SMGs) in the Extended *Chandra* Deep Field South. Strong detections of ^{12}CO(1–0) emission from two SMGs, ALESS 122.1 ($z = 2.0232$) and ALESS 67.1 ($z = 2.1230$), were obtained. We estimate gas masses of $M_{\rm gas} \sim 1.3 \times 10^{11}$ M$_\odot$ and $M_{\rm gas} \sim 1.0 \times 10^{11}$ M$_\odot$ for ALESS 122.1 and ALESS 67.1, respectively, adopting $\alpha_{\rm CO} = 1.0$. Dynamical mass estimates from the kinematics of the ^{12}CO(1–0) line yields $M_{\rm dyn}\ \sin^2\ i = (2.1 \pm 1.1) \times 10^{11}$ M$_\odot$ and $(3.2 \pm 0.9) \times 10^{11}$ M$_\odot$ for ALESS 122.1 and ALESS 67.1, respectively. This is consistent with the total baryonic mass estimates of these two systems. We examine star formation efficiency, using the $L_{\rm FIR}$ versus $L'_{\rm CO(1-0)}$ relation for samples of local ultraluminous infrared galaxies (ULIRGs) and Luminous Infrared Galaxies (LIRGs), and more distant star-forming galaxies, with ^{12}CO(1–0) detections. We find some evidence of a shallower slope for ULIRGs and SMGs compared to less luminous systems, but a larger sample is required for definite conclusions. We determine gas-to-dust ratios of 170 ± 30 and 140 ± 30 for ALESS 122.1 and ALESS 67.1, respectively, showing that ALESS 122.1 has an unusually large gas reservoir. By combining the 38.1 GHz continuum detection of ALESS 122.1 with 1.4 and 5.5 GHz data, we estimate that the free–free contribution to radio emission at 38.1 GHz is 34 ± 17 μJy, yielding a star formation rate (1400 ± 700 M$_\odot$ yr^{-1}) consistent with that from the infrared luminosity.

Key words: galaxies: evolution – radio lines: galaxies – submillimetre: galaxies.

1 INTRODUCTION

Since their initial discovery, submillimetre galaxies (SMGs) have become an important element of our understanding of cosmic galaxy formation and evolution (e.g. Blain et al. 2002; Casey, Narayanan & Cooray 2014). Selected in the rest-frame far-infrared (FIR), SMGs contain significant masses of cold dust (Casey et al. 2012) and large reservoirs of molecular gas ($\gtrsim 10^{10}$ M$_\odot$; e.g. Bothwell et al. 2013). These luminous galaxies have median redshifts of $z \sim 2$–3 (Chapman et al. 2005; Wardlow et al. 2011; Smolčić et al. 2012; Simpson et al. 2014), and extreme FIR luminosities $L_{\rm FIR} > 10^{12}$ L$_\odot$ implying large star formation rates (SFRs) of ∼100–1000 M$_\odot$ yr^{-1} (e.g. Blain et al. 2002). The peak of star formation (SF) in the Universe also occurred at $z \sim 2$–3 (Hopkins & Beacom 2006; Madau & Dickinson 2014) and ultraluminous infrared galaxies (ULIRGs) are responsible for roughly half of the cosmic infrared luminosity density at those redshifts (Gruppioni et al. 2013; Magnelli et al. 2013), suggesting that SMGs play a vital role in galaxy evolution.

Since the extreme SFRs of local ULIRGs are believed to be driven by major mergers, it has also been asserted that SMGs at high redshift have similar evolutionary histories (e.g. Engel et al. 2010; Chen et al. 2015). However, secular origins have also been proposed for SMGs, with one justification being that there are not enough mergers in some simulations to account for the number of observed SMGs (e.g. Hopkins & Hernquist 2010; Hayward et al. 2013). Cosmological hydrodynamic simulations are now able to reproduce some SMG properties, such as stellar masses and molecular gas

★ E-mail: minh.huynh@uwa.edu.au

fractions, without a major merger (e.g. Davé et al. 2010; Narayanan et al. 2015), but they in general cannot reproduce the highest SFRs seen in SMGs or match the properties of descendants at $z \sim 0$. Moreover, the SMG population appears to be diverse, and so large observational samples are necessary to capture this diversity and test the models.

Molecular gas studies of SMGs provide unique insight into the physical properties of these systems. Molecular line observations provide information on the kinematics of the galaxy (i.e. turbulent versus ordered rotating discs), as well as dynamical and gas mass estimates. Radio emission produced by the rotational transition of carbon monoxide (^{12}CO) is one of the most accessible tracers of cold molecular gas in galaxies (Carilli & Walter 2013). However, only a few tens of unlensed SMGs at $z \gtrsim 1.5$ have been detected in CO (e.g. Carilli & Walter 2013) and most are of high-J ($J > 2$) transitions. The high-CO transitions trace dense and thermally excited gas in the starburst/AGN regions, while only the lowest CO transitions fully reveal the more widely distributed reservoirs of less dense, subthermally excited gas (e.g. Papadopoulos & Allen 2000; Papadopoulos et al. 2001; Carilli et al. 2010; Ivison et al. 2011). The ground transition CO(1–0) is least affected by the excitation conditions of the gas and therefore provides the most robust estimates of overall molecular gas content and the broadest tracer of the dynamics of the system.

To study the molecular gas content of SMGs, we have initiated a survey of CO(1–0) with the Australia Telescope Compact Array (ATCA). We describe the SMG sample and the ATCA observations in Section 2. The results of the observations are presented in Section 3. In Section 4, we discuss the molecular gas masses, dynamical masses, SF efficiency and dust-to-gas ratios of the observed systems. The standard ΛCDM cosmological parameters of $\Omega_{\rm M} = 0.29$, $\Omega_{\Lambda} = 0.71$ and a Hubble constant of 70 km s^{-1} Mpc^{-1} are adopted throughout this paper.

2 OBSERVATIONS AND DATA REDUCTION

2.1 Our ALESS SMG sample

Our sample is selected from the ALMA study of 99 submillimetre sources from the ALMA LABOCA Extended *Chandra* Deep Field South (ECDFS) Submillimetre Survey (ALESS; Weiß et al. 2009; Hodge et al. 2013). ALESS is an ALMA Cycle 0 survey at 870 μm to follow up 122 of the original 126 submm sources detected by the LABOCA ECDFS Submillimeter Survey (LESS; Weiß et al. 2009). The excellent angular resolution and sensitivity of ALMA (∼1.5 arcsec and about three times deeper than LESS) resulted in a sample of 99 statistically reliable SMGs (Hodge et al. 2013). This large ALMA-identified SMG sample is free of the biases and misidentifications that have affected previous SMG studies.

The ECDFS (RA = 03$^{\rm h}$32$^{\rm m}$28$^{\rm s}$, Dec = −27°48′30″) is one of the best studied extragalactic survey fields available, allowing for secure identification of counterparts at other wavelengths. A spectroscopic survey of the original LESS SMGs was performed as part of a Very Large Telescope (VLT) Large Programme with the FOcal Reducer and low dispersion Spectrograph (FORS2) and VIsible MultiObject Spectrograph (VIMOS) during 2009–2012 (Danielson et al. 2016). To supplement the Large Programme, and target ALMA-identified ALESS SMGs that differed from the original LESS counterparts, observations were also obtained on XSHOOTER on the VLT, Gemini Near-Infrared Spectrograph on Gemini South, the Multi-Object Spectrometer for Infra-Red Exploration on Keck I and DEep Imaging Multi-Object Spectrograph on Keck II. This extensive spectroscopic campaign has provided secure redshifts for 51/99 ALESS SMGs (Danielson et al. 2016). *Herschel* Spectral and Photometric Imaging Receiver (SPIRE) imaging was deblended by combining the ALMA, *Spitzer* Multiband Imaging Photometer 24 μm and radio catalogue priors, to determine FIR properties, including dust masses, total infrared luminosities and SFRs of the individual SMGs (Swinbank et al. 2014).

Our initial sample consists of nine ALESS SMGs at $1.5 < z < 2.5$, where CO(1–0) is detectable in the ATCA 7 mm band, with the best-quality optical spectra from Danielson et al. (2016). These nine SMGs have secure redshifts with multiple emission or absorption features identified in the optical spectra. Pilot ATCA observations were granted in the 2015 OCT semester in which we targeted two ALESS SMGs: ALESS 122.1 and ALESS 67.1. These two targets were chosen as they are the most infrared-luminous SMGs out of the nine, and hence most likely to have detectable molecular gas reservoirs.

2.2 ATCA observations and data reduction

Observations of ALESS 122.1 and ALESS 67.1 were performed on the ATCA, using the Compact Array Broadband Backend (CABB; Wilson et al. 2011), in 2015 August and September. The array was in the standard compact hybrid configurations H75 and H168 for ALESS 122.1 and ALESS 67.1, resulting in maximum baselines of 89 and 192 m, respectively, discarding the outer sixth antenna. The hybrid configurations, consisting of two antennas along the northern spur, allow good (u, v) coverage to be obtained for integrations less than the full 12-h synthesis. Our observations consisted of ∼8-h runs to ensure the source elevation is greater than ∼30 deg. We obtained total integration times of 38 and 31-h on-source for ALESS 122.1 and ALESS 67.1, respectively. The weather was good to average, with atmospheric path length rms variations generally in the range of 50–400 μm, as measured on the 230 m baseline ATCA Seeing Monitor (Middelberg, Sault & Kesteven 2006). The 7 -mm receiver was centred at the expected frequency of the ^{12}CO(1–0) line emission ($\nu_{\rm rest}$ = 115.2712 GHz), given their spectroscopic redshifts, i.e. 38.129 GHz for ALESS 122.1 and 36.910 GHz for ALESS 67.1 GHz. The 2GHz bandwidth of CABB results in a velocity coverage of approximately 15 000 km s^{-1}.

Following Emonts et al. (2011), a bandpass calibration scan was acquired at the beginning and end of each 8-h night; however, we found that the bandpass scan in the beginning of the night is sufficient for good bandpass calibration and the second scan is thus a backup. Phase and amplitude calibration information was acquired with 2-min scans on PKS 0346−279 every 15 min and pointing checks performed on the same source every hour. For flux calibration, we observed Uranus at a time when it was close to the same elevation as our targets; this occurred around 00:30 LST and at an elevation of ∼50 deg. The uncertainty in the flux density calibration using the standard MIRIAD model of Uranus is estimated to be 30 per cent (Emonts et al. 2011), but can be as little as 20 per cent when following this scheme and in good conditions.

The data were calibrated, mapped and analysed using the standard MIRIAD (Sault & Killeen 1999) and KARMA (Gooch 1996) packages. The synthesized beam from natural weighting is 14.4 × 10.6 arcsec and 7.0 × 4.6 arcsec for ALESS 122.1 and ALESS 67.1, respectively. The resultant noise in the single 1 MHz (∼8 km s^{-1}) channels is ∼0.40 mJy beam^{-1} for both the ALESS 122.1 and ALESS 67.1 cubes, consistent with other comparable 7 mm ATCA/CABB studies (e.g. Coppin et al. 2010; Emonts et al. 2014, 2015; Huynh et al. 2014).

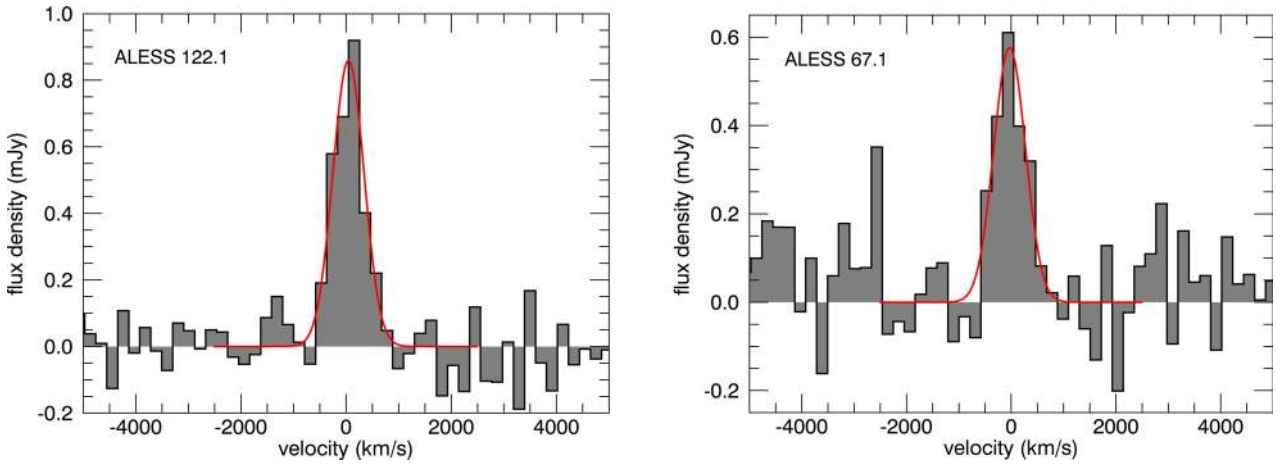

Figure 1. The CO(1–0) spectrum for ALESS 122.1 (left, continuum subtracted) and ALESS 67.1 (right), binned to 200 km s^{-1} resolution. The best-fitting Gaussian is shown as a red line. The CO emission peaks at $\gtrsim 8\sigma$ significance with this binning with both lines well fit by single Gaussians at this resolution.

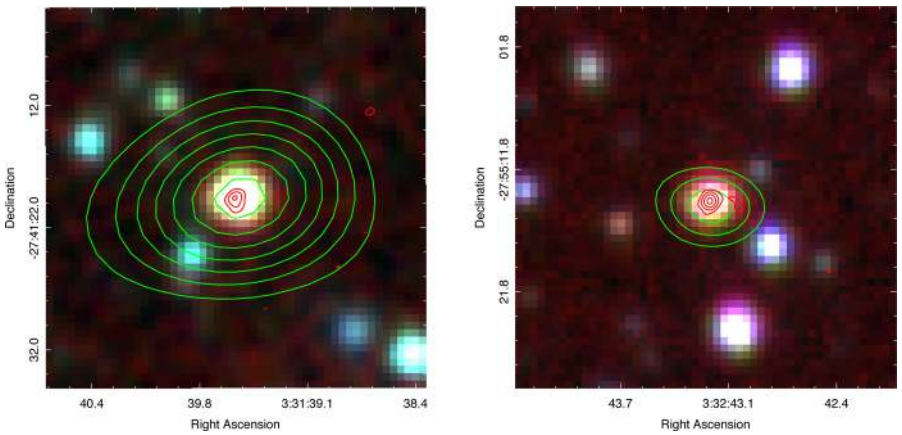

Figure 2. False-colour images made from *Spitzer* Infrared Array Camera (IRAC) images of Damen et al. (2011)[1] for ALESS 122.1(left) and ALESS 67.1 (right). Green contours indicate the CO(1–0) emission from the 600 km s^{-1} cube at 3, 5, 7... $\times\,\sigma$. The red contours are from the ALMA 870 μm continuum map (Hodge et al. 2013) at 3, 5, 7... $\times\,\sigma$. The postage stamp images are 30 × 30 arcsec.

3 RESULTS

The visibilities were resampled to produce cubes with velocity resolutions of 200, 300, 400 and 600 km s^{-1} and each cube was examined for an emission line at the expected redshift and centred near the ALMA position. We identify a line at the ALMA position and spectroscopic redshift in the cubes for both sources at more than 8σ significance, and across multiple channels for 200 and 300 km s^{-1} binning. The 200 km s^{-1} binned spectra have similar sensitivities (0.079 mJy beam^{-1}) and the CO peaks are detected at $\sim 12\sigma$ and $\sim 8\sigma$ significance in the brightest channel for ALESS 122.1 and ALESS 67.1, respectively (see Fig. 1). The CO emission is coincident with the ALMA submillimetre source and has a clear IRAC counterpart (Fig. 2).

Gaussian fits were performed on the 200 km s^{-1} cube to obtain ^{12}CO(1–0) line parameters, which are summarized in Table 1. The CO(1–0) spectrum for ALESS 122.1 has a significant fitted continuum of 70 ± 20 μJy, which is subtracted from the spectra in Fig. 1. The CO(1–0) line for ALESS 122.1 then has a fitted peak of 0.86 ± 0.06 mJy, a full width at half-maximum (FWHM) of 700 ± 60 km s^{-1}. The CO(1–0) line for ALESS 67.1 has a fitted peak of 0.58 ± 0.07 mJy and an FWHM of 710 ± 90 km s^{-1}. Both lines are consistent with having a zero velocity offset with respect to the optical spectroscopic redshift. Integrating the best-fitting Gaussian yields a line luminosity of 0.64 ± 0.07 and 0.44 ± 0.08 Jy km s^{-1} for ALESS 122.1 and ALESS 67.1, respectively. These values do not include the flux calibration uncertainties, which are about 20–30 per cent (Emonts et al. 2011).

Continuum images were also made from the full CABB 2 GHz bandwidth for each SMG. The central 200 channels were flagged to remove any CO(1–0) flux, and natural weighting used to achieve the highest sensitivity. Both SMGs are detected in the continuum images as point sources, with ALESS 122.1 having a 38.1 GHz flux density of 60 ± 10 μJy and ALESS 67.1 having a 36.9 GHz flux density of 48 ± 11 μJy.

4 ANALYSIS AND DISCUSSION

4.1 Molecular gas masses

CO detections provide a tool for deriving the masses of the molecular gas reservoirs of these systems. This is important as the reservoir of molecular gas is the raw material from which new stars will be

[1] https://irsa.ipac.caltech.edu/data/SPITZER/SIMPLE/

Table 1. Observed and derived properties of ALESS 122.1 and ALESS 67.1.

	ALESS 122.1	ALESS 67.1
$RA_{CO(1-0)}$ (J2000)	03:31:39.53	03:32:43.20
$Dec_{CO(1-0)}$ (J2000)	−27:41:19.6	−27:55:14.8
z_{spec}	2.0232	2.1230
$z_{CO(1-0)}$	2.0238 ± 0.0003	2.1228 ± 0.0004
L_{FIR}[a] (10^{12} $L_\odot$)	$6.3^{+0.4}_{-0.5}$	$5.3^{+0.7}_{-1.3}$
SFR[b] ($M_\odot$ yr^{-1})	940^{+60}_{-80}	790^{+100}_{-190}
M_{dust}[a] (10^8 $M_\odot$)	7.9 ± 0.9	7.1 ± 0.6
Dust temperature[a] (K)	32	31
$peak_{CO(1-0)}$ (mJy)	0.86 ± 0.06	0.58 ± 0.07
$FWHM_{CO(1-0)}$ (km s^{-1})	700 ± 60	710 ± 90
CO(1–0) line centre (km s^{-1})	45 ± 30	−31 ± 40
$I_{CO(1-0)}$ (Jy km s^{-1})	0.64 ± 0.07	0.44 ± 0.08
$L'_{CO(1-0)}$ (10^{10} K km s^{-1} pc^2)	13 ± 2	9.9 ± 1.8
$M(H_2)$ (10^{10} $M_\odot$)[c]	13 ± 2	9.9 ± 1.8
$S_{7\,mm\,continuum}$ (μJy)	60 ± 10	48 ± 11

Notes. [a]from Swinbank et al. (2014).
[b]using L_{FIR} conversion from Kennicutt & Evans (2012).
[c]Adopting $\alpha_{CO} = 1$.

formed, thus giving an indication of the final mass of these systems post the starburst phase (modulo gas falling into or being ejected from the system). The ground transition of CO(1–0) is particularly powerful as no assumption of a brightness ratio, or gas spectral line energy distribution, is required to convert down from a higher J transition.

Following the method of Solomon & Vanden Bout (2005), we find that ALESS 122.1 has a line luminosity of $L'_{CO(1-0)} = (1.3 \pm 0.2) \times 10^{11}$ K km s^{-1} pc^2 and ALESS 67.1 has a line luminosity of $L'_{CO(1-0)} = (9.9 \pm 1.8) \times 10^{10}$ K km s^{-1} pc^2 (Table 1). A CO-to-H_2 conversion factor, α_{CO}, is then required to convert the line luminosity to a total molecular gas mass, $M(H_2)$. At $z \sim 0$ disc galaxies such as the Milky Way have relatively large values of $\alpha_{CO} \sim 3$–5, while a smaller value of $\alpha_{CO} = 0.8$ is believed to be appropriate for local ULIRGs (e.g. Downes & Solomon 1998), and this has been widely used for high-redshift SMGs. However, there is some evidence that the local ULIRG value of $\alpha_{CO} = 0.8$ leads to underestimated gas masses (Bothwell et al. 2010) and at least one SMG is known to have a large $\alpha \sim 2$ (Danielson et al. 2011; Swinbank et al. 2011). Given the uncertainty in the conversion factor, we adopt $\alpha_{CO} = 1$, following Bothwell et al. (2013), and derive molecular gas masses, $M(H_2)$, of $(1.3 \pm 0.2) \times 10^{11}$ $M_\odot$ and $(9.9 \pm 1.8) \times 10^{10}$ $M_\odot$ for ALESS 122.1 and ALESS 67.1, respectively. The mean gas mass for a representative sample of $z \sim 2$ SMGs from $J \gtrsim 3$ observations has been found to be $(3.2 \pm 2.1) \times 10^{10}$ $M_\odot$ (Bothwell et al. 2013). The high-J transitions used in the earlier work may explain some of the discrepancy, but nevertheless ALESS 122.1 and ALESS 67.1 appear to have relatively large gas masses compared to the general SMG population. This is not unexpected as they were selected to have large IR luminosities.

4.2 CO line kinematics and dynamical masses

The kinematics of the CO line traces the gravitational potential well in the system. Previous studies have found very broad CO emission lines from SMGs, but are typically from $J \gtrsim 3$ transition lines. Bothwell et al. (2013) find a mean FWHM of 510 ± 80 km s^{-1} for their sample of SMGs. A greater mean FWHM of 780 km s^{-1} was found for a more infrared-luminous subset of those SMGs (Greve et al. 2005). More infrared-luminous sources could potentially have a greater dynamical mass, and therefore a larger CO line FWHM. The CO line FWHMs of ALESS 122.1 and ALESS 67.1 are ∼700 km s^{-1}, which are larger than most of the Bothwell et al. (2013) SMG sample, but in line with what is expected from the more infrared-luminous SMGs. The measured CO(1–0) linewidth may also be relatively large due to the $J = 1$–0 transition being more spatially extended than higher J transitions (e.g. Ivison et al. 2011; Emonts et al. 2015).

The width of the CO line from the SMGs allows an estimation of the galaxy dynamical masses, given a spatial extent of the system and an assumption about the dynamical structure. Following Solomon & Vanden Bout (2005), the dynamical mass of the system can be estimated using M_{dyn} $\sin^2$ $i = 233.5\,V^2R$, where R is the radius of the molecular disc or half the separation between components in a merger model, measured in parsec, and V is the FWHM of the CO line or half the separation in velocity of the component CO lines in a merger model, measured in km s^{-1}. The *HST* images (Rix et al. 2004) show various clumps that indicate ALESS 122.1 and ALESS 67.1 could be mergers (Fig. 3). Taking the merger model and R to be $\lesssim$0.5 arcsec (4.2 kpc at $z = 2$), which is the approximate separation of the clumps in *HST* optical counterparts (Fig. 3), the dynamical mass, M_{dyn} $\sin^2$ i, is $\lesssim 5 \times 10^{11}$ $M_\odot$ for both ALESS 122.1 and ALESS 67.1.

However, the *HST* image does not reveal whether or not the systems contain a gaseous disc. In the presence of a gas disc, the dynamical mass can be estimated from the CO line kinematics, by comparing the spatial offset between the redshifted and blueshifted components of the CO line. This was determined by making 300 km s^{-1} wide channel maps centred at −300 to 0 km s^{-1} and 0 to +300 km s^{-1} (Fig. 3). The centroid of the CO emission was determined for the maps, and we derive a spatial offset between the redshifted and blueshifted emissions of 1.2 ± 0.6 arcsec (10.2 ± 5.1 kpc) and 1.8 ± 0.5 arcsec (15.2 ± 4.2 kpc) for ALESS 122.1 and ALESS 67.1, respectively. This is comparable to CO(1–0) sizes observed in other SMGs by Ivison et al. (2011). Assuming this spatial offset represents rotating gas, then the dynamical mass M_{dyn} $\sin^2$ $i = (2.1 \pm 1.1) \times 10^{11}$ $M_\odot$ and $(3.2 \pm 0.9) \times 10^{11}$ $M_\odot$ for ALESS 122.1 and ALESS 67.1, respectively. These estimates are consistent with the dynamical masses derived from using the CO line FWHM and optical size from *HST* imaging. For a rotating model, Bothwell et al. (2013) found their sample of SMGs to have a median dynamical mass of $(1.6 \pm 0.3) \times 10^{10}$ R $M_\odot$, where radius R is in kpc. Using the measured spatial offsets of 10 and 15 kpc for R, the dynamical masses of ALESS 122.1 and ALESS 67.1 are consistent with the median dynamical mass of their SMG sample.

The total baryonic mass can be calculated by combining the gas and stellar mass estimates for the SMGs. The stellar masses of ALESS 122.1 and ALESS 67.1 have been estimated by Simpson et al. (2014), who used absolute rest-frame H-band magnitudes from best-fitting SEDs to multiband photometry and a model mass-to-light ratio. They estimate ALESS 122.1 has a stellar mass of 5.2×10^{10} $M_\odot$ and ALESS 67.1 has a stellar mass of 4.4×10^{10} $M_\odot$. These estimates are uncertain by a factor of at least a few, due to the difficulty in distinguishing between different model SF histories to predict an accurate mass-to-light ratio (Hainline et al. 2011). Nevertheless, this suggests that the total baryonic mass of the system, $M_{bary} = M_{H_2} + M_{stars}$, is then $(1.9 \pm 1.1) \times 10^{11}$ $M_\odot$ and $(1.4 \pm 0.9) \times 10^{11}$ $M_\odot$ for ALESS 122.1 and ALESS 67.1, respectively, where the uncertainties for the stellar mass estimate

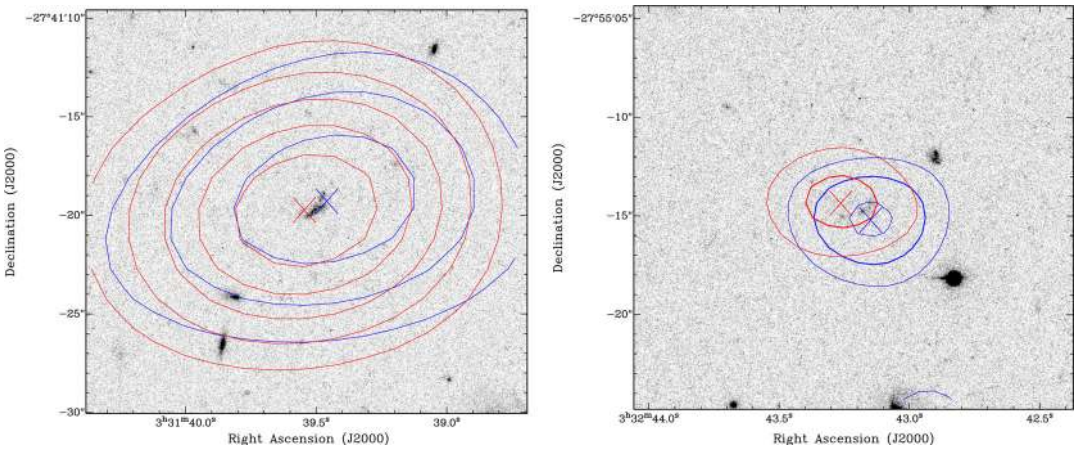

Figure 3. The CO(1–0) velocity structure of ALESS 122.1 (left) and ALESS 67.1 (right), overlaid on *HST* z band (*F*850*LP*) images from Rix et al. (2004)[3]. Both optical counterparts are clumpy or complex in the rest-frame UV, indicating either structured dust or a possible merging system. Blue contours indicate the CO(1–0) emission integrated from −300 to 0 km s^{-1} at 3, 5, 7... × σ. Red contours indicate the CO(1–0) emission integrated from 0 to +300 km s^{-1} at 3, 5, 7... × σ. Red and blue crosses mark the centroid of the blueshifted and redshifted emission, respectively. The images are 20 × 20 arcsec.

are assumed to be a factor of 2. These mass estimates are consistent with the derived dynamical masses, given the uncertainties involved. Given these total baryonic mass estimates, ALESS 122.1 and ALESS 67.1 have gas mass fractions of ∼70 per cent, which, although large, have been observed in other gas-dominated SMGs (e.g. Bothwell et al. 2013) and $z \sim 2$ UV-selected massive star-forming galaxies (Tacconi et al. 2010).

4.3 Star formation efficiency

The detection of CO(1–0) provides an opportunity to examine the efficiency with which the molecular gas is being converted into stars in these systems. SF efficiency is commonly defined as SFR/$M(H_2)$, the inverse of the gas depletion time-scale. A useful approach is to investigate the SF efficiency by comparing the two observable quantities, total infrared luminosity L_{FIR} and line luminosity $L'_{CO(1-0)}$. Using these observables instead negates any offsets in SFR/$M(H_2)$ that may be introduced by the application of an inappropriate CO-to-H_2 conversion factor α_{CO}. The slope of the L_{FIR}–$L'_{CO(1-0)}$ relation describes the relationship between the infrared luminosity due to SF and the total gas content of the system. It is thus a basic observational form of the Kennicutt–Schmidt (K-S) relation between the gas reservoir and the SFR of a system.

The original form of the K-S relation was established using H I and CO(1–0) measurements of galaxies in the local universe (Schmidt 1959; Kennicutt 1989, 1998) and the SFR density was found to be related to gas surface density by a power law, $\Sigma_{SFR} \propto \Sigma_{gas}^{N}$, with the slope $N = 1.4 \pm 0.15$ (Kennicutt 1998). Using the COLD GASS sample of about 350 local massive galaxies, Saintonge et al. (2012) find a global K-S relation of $N = 1.18 \pm 0.24$. At higher redshifts ($z \sim 1-3$), Genzel et al. (2010) suggested that 'normal' star-forming galaxies show a K-S relation of $N = 1.17 \pm 0.09$ and SMGs show a similar slope of $N = 1.1 \pm 0.2$ but offset by 1 dex above the 'normal' star-forming galaxies. Their result comes from high-J (mostly $J = 3$) transitions of CO, however, and different α_{CO} are adopted for the different populations included in their study.

The 'integrated' K-S relation, as opposed to the original 'surface density' K-S relation, is also observed, but assumes the SF (e.g. as measured by the FIR), has the same spatial extent as the molecular gas. In the L_{FIR} and $L'_{CO(1-0)}$ plane 'normal' star-forming galaxies show a slope[2] of 1.15 ± 0.12 and SMGs have a similar slope but offset on average by a factor of 4 above the relation for 'normal' star-forming galaxies (Genzel et al. 2010). Since the $L'_{CO(1-0)}$ luminosities of the 'normal' star-forming galaxies extended into the bright SMG regime ($\gtrsim 10^{10}$ K km s^{-1} pc^2), Genzel et al. (2010) argued this is evidence that the merging populations (ULIRG and SMG) are offset from the 'normal' $z = 0$ disc galaxy population, rather than a change of slope occurring at high luminosities. More recent work on (local) ULIRGs and SMGs found an L_{FIR}–$L'_{CO(1-0)}$ relation slope of 1.20 ± 0.09 for the populations combined, and 1.27 ± 0.08 and 1.08 ± 0.14 for the ULIRG and SMG populations, respectively (Bothwell et al. 2013). These studies relied on $J = 2$ or higher transitions of CO converted to CO(1–0), introducing systematic uncertainties in the relation. Ivison et al. (2011) used mostly CO(1–0) transitions and fully self-consistent L_{FIR} measurements to find a shallower slope of 0.65 ± 0.13 for SMGs, suggesting that high transitions of CO may artificially steepen the slope.

With new CO(1–0) detections of SMGs and BzKs over the last few years, and now our work, we can make a relatively unbiased comparison to local samples. In Fig. 4, we show L_{FIR} and $L'_{CO(1-0)}$, populated with local ULIRGs from Solomon et al. (1997) and Chung et al. (2009), and local LIRGs from Papadopoulos et al. (2012). For 'normal' star-forming galaxies at $z \sim 2$, we include eight BzK galaxies with published CO detections (Aravena et al. 2010, 2012; Daddi et al. 2010), all but three in CO(1–0). Three BzKs have only CO(2–1) detections, which Daddi et al. (2010) correct to $L'_{CO(1-0)}$ adopting $r_{21} = 0.84$. This is also the median r_{21} ratio found by Bothwell et al. (2013), so we include the Daddi et al. (2010) CO(2–1) detections with the corrected $L'_{CO(1-0)}$. SMGs with CO(1–0) detections come from Greve, Ivison & Papadopoulos (2003), Ivison et al. (2011), Swinbank et al. (2011) and Harris et al. (2012). Because of the small number of SMGs detected in CO(1–0) (21 including this work), we add seven Bothwell et al. (2013) SMGs with CO(2–1) detections, where $L'_{CO(1-0)}$ is derived using $r_{21} = 0.84$. Care was taken in the compilation to use a consistent definition of L_{FIR} across the samples. In the literature, total infrared luminosity L_{FIR} is usually the luminosity across 8–1000 μm, but in some cases, especially

[2] Here slope is a, where $L_{FIR} \propto L'^{a}_{CO(1-0)}$.
[3] https://archive.stsci.edu/prepds/gems/

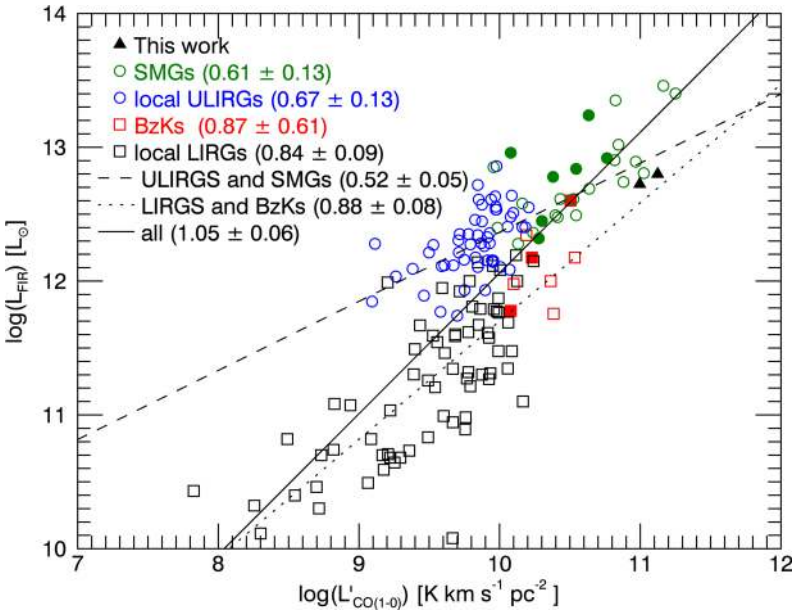

Figure 4. $L_{\rm FIR}$ versus $L'_{\rm CO(1-0)}$ for SMGs, local (U)LIRGs and BzK galaxies. All sources but three BzKs (filled squares) and seven SMGs (filled circles) have robust CO(1–0) measurements. The filled squares and circles mark sources with CO(2–1) detections that are converted to CO(1–0) using $r_{21} = 0.84$. Linear relations are fitted to the local ULIRGs plus SMGs (dashed) and local LIRGs plus BzK galaxies (dotted), as well as all the samples combined (solid). The numbers in brackets indicate the bestfitting slope for the different populations.

IRAS samples, authors have given the luminosity across 42.5–122.5 μm. In these cases (Solomon et al. 1997; Chung et al. 2009), we convert the quoted infrared luminosity to L(8–1000 μm), using a factor of 1.9, consistent with typical infrared SEDs (e.g. Helou et al. 1988; Chary & Elbaz 2001).

A linear relation of the form $\log L_{\rm FIR} = a \log L'_{\rm CO(1-0)} + b$ was fitted with chi-square minimization, using the MPFITEXY routine (Williams, Bureau & Cappellari 2010) to take into account errors in both coordinates. The slopes, a, were determined for the various samples, and we report these in the legend of Fig. 4. The local ULIRGs and SMGs have consistent slopes of $a = 0.67 \pm 0.13$ and $a = 0.61 \pm 0.13$, respectively. The more normal star-forming galaxy samples, local LIRGs and BzKs, show marginally steeper slopes of $a = 0.84 \pm 0.09$ and $a = 0.87 \pm 0.61$, but the BzK slope is highly uncertain due to the small number of sources in that sample and the limited luminosity range spanned. The combined BzK and LIRG sample exhibits a slope of $a = 0.88 \pm 0.08$, which is steeper than the ULIRG and SMG combined slope of $a = 0.52 \pm 0.05$ at about the 2σ significance level. While a larger sample of SMGs and BzKs with well-determined line luminosities $L'_{\rm CO(1-0)}$ is required to definitively say that ULIRGs and SMGs populate a different sequence in the K-S relation to the more normal LIRGs and BzKs, this work does hint that there may be a difference in their SF modes. We stress that our analysis is free of the biases from high-J CO transitions that has been present in earlier work (e.g. Greve et al. 2005; Daddi et al. 2010; Genzel et al. 2010). By using the CO(1–0) transition (and CO(2–1) for a small number of sources), we remove the uncertainties in the line luminosity introduced by excitation conditions of the gas.

The total infrared luminosities of ALESS 122.1 and ALESS 67.1 (Swinbank et al. 2014) correspond to SFRs of 940^{+60}_{-80} and 790^{+100}_{-190} $M_\odot$ yr^{-1}, respectively, using the infrared conversion from Kennicutt & Evans (2012). The gas depletion time-scales, $M(H_2)$/SFR, are 140 ± 30 and 130 ± 40 Myr, which are similar to other SMGs at $z \sim 2$ (e.g. Bothwell et al. 2013). Assuming little further gas infall from the surrounding environment and 100 per cent efficiency in converting the gas to stars, the SF is effectively shut off at $z \sim 2$ and this galaxy would appear as a 'red and dead' elliptical by $z \sim 1.5$ (1 Gyr after gas depletion). The estimated total baryonic masses ($>1 \times 10^{11}$ $M_\odot$) and time-scales involved are consistent with these SMGs being progenitors of today's massive ellipticals, which has been the consensus in the literature for some time (e.g. Lilly et al. 1999; Simpson et al. 2014).

4.4 Dust-to-gas mass ratios

As early as the 1980s, it was suggested that the emission from dust could be used to measure the mass of the interstellar medium (ISM) in a galaxy (Hildebrand 1983). Dust mass estimates can be determined from the infrared-submm luminosity on the Rayleigh–Jeans tail of the dust SED, and then an appropriate gas-to-dust ratio can be applied to derive the total mass of the molecular ISM (Eales et al. 2012; Scoville et al. 2014). *Herschel* surveys have catalogued hundreds of thousands of galaxies (e.g. *Herschel*-ATLAS; Eales et al. 2010; Valiante et al. 2016) in the FIR, and SCUBA2 has detected thousands of galaxies in the submm (SCUBA2 Cosmology Legacy Survey; Geach et al. 2017). Individual CO measurements cannot feasibly be made for all of these galaxies, but dust mass estimates provide a potential avenue for crudely estimating total gas masses for very large samples of galaxies.

The Milky Way has a gas-to-dust ratio of $\delta_{\rm GDR} \sim 130$ (Jenkins 2004), while the *Spitzer* Infrared Nearby Galaxy Survey (SINGS) of 13 local star-forming galaxies have $\delta_{\rm GDR} = 130 \pm 20$ (Draine et al. 2007). Combining the CO-derived gas measurements from Bothwell et al. (2013) and dust mass estimates from FIR SEDs by Magnelli et al. (2012), the average $\delta_{\rm GDR}$ for SMGs is estimated to be 90 ± 25 (Swinbank et al. 2014). Combining the dust mass estimates of ALESS 122.1 and ALESS 67.1 from Swinbank et al. (2014) with our CO(1–0) gas mass estimates results in gas-to-dust ratios $\delta_{\rm GDR} = 170 \pm 30$ and 140 ± 30, respectively. This suggests

that ALESS 122.1 has an unusually large gas-to-dust ratio, probably due to its extremely large gas reservoir.

The monochromatic submm flux density has been explored as a probe of gas mass. It potentially provides a simple and effective estimate of both the dust and gas mass content of a galaxy. *Planck* measurements of the submillimetre emission from Milky Way regions yield a Galactic constant of proportionality between 850-μm luminosity and ISM mass of $\alpha = L_{850}/M_{\rm ISM} = 0.79 \times 10^{20}$ erg s^{-1} Hz^{-1} M$_\odot^{-1}$, while an empirical calibration using 12 local ULIRGs and SINGS survey galaxies yields $\alpha = 1.0 \pm 0.2 \times 10^{20}$ erg s^{-1} Hz^{-1} M$_\odot^{-1}$ (Scoville et al. 2014). We convert the measured ALMA 870-μm continuum flux densities of ALESS 122.1 and ALESS 67.1 (Hodge et al. 2013) to 870-μm rest-frame luminosities following

$$L_{870} = 4\pi D^2 (1+z) S_{870} K_{\rm corr},$$

where L_{870} is the luminosity in W Hz^{-1}, D is the comoving distance, S_{870} is the observed flux density at 870 μm and $K_{\rm corr}$ is the K-correction that is given by

$$K_{\rm corr} = \left(\frac{\nu_{\rm obs}}{\nu_{\rm obs(1+z)}}\right)^{3+\beta} \frac{e^{h\nu_{\rm obs(1+z)}/kT} - 1}{e^{h\nu_{\rm obs}/kT} - 1},$$

where $\nu_{\rm obs}$ is the observed ALMA frequency (350 GHz), $\nu_{\rm obs(1+z)}$ is the rest-frame frequency, T is the dust SED effective temperature and β is the dust emissivity index. We use temperatures of 32 and 31 K for ALESS 122.1 and ALESS 67.1, respectively, which have been determined from the detailed FIR SED fitting of Swinbank et al. (2014). The emissivity index β can range from 1.5 to 2.0, but for consistency with Scoville et al. (2014), we take $\beta = 1.8$. We thus find $L_{850} = (1.0 \pm 0.1) \times 10^{31}$ erg s^{-1} Hz^{-1} for ALESS 122.1 and $L_{850} = (1.3 \pm 0.1) \times 10^{31}$ erg s^{-1} Hz^{-1} for ALESS 67.1. This corresponds to monochromatic 850 μm luminosity-to-mass ratios of (0.75 ± 0.11) and $(1.3 \pm 0.3) \times 10^{20}$ erg s^{-1} Hz^{-1} M$_\odot^{-1}$ for ALESS 122.1 and ALESS 67.1, respectively, using our measured CO molecular gas masses. This is consistent with the result from Scoville et al. (2014) given that the uncertainty in the luminosity-to-mass ratios includes only the flux uncertainties for the CO and ALMA measurements. The luminosity-to-mass ratio given by Scoville et al. (2014) includes H I masses, which we do not include here, and that will also add some uncertainty to the ratio.

4.5 Radio thermal free–free emission and the SFR

Most radio measures of SF use non-thermal radio synchrotron radiation (e.g. Haarsma et al. 2000; Seymour et al. 2008), which is emitted by cosmic ray electrons propagating through a galaxy's magnetic field after being initially accelerated by core-collapse supernovae. This synchrotron emission is a complex tracer of SF and is potentially affected by the inverse-Compton losses against the Cosmic Microwave Background (CMB), which scales as $(1+z)^4$. The thermal free–free radio emission from ionized H II regions traces the massive young stars (>5 M$_\odot$) that are capable of photoionizing the ISM. As such, it is a more direct tracer of the SFR of a galaxy than synchrotron radio emission, and has the same advantage of being a dust-unbiased indicator. The thermal fraction at GHz frequencies for a typical star-forming galaxy is $\lesssim$10 per cent but thermal emission dominates by about 30 GHz (Condon 1992).

ALESS 122.1 is detected at 1.4 GHz (Miller et al. 2013) and 5.5 GHz (Huynh et al. 2015), with flux densities of 202.6 ± 14.1 and 71 ± 9 μJy, respectively. Combined with our high-frequency 38.1 GHz continuum detection, we can make an estimate of the amount of radio free–free emission in ALESS 122.1. The free–free luminosity is derived by fitting the radio SED with a fixed

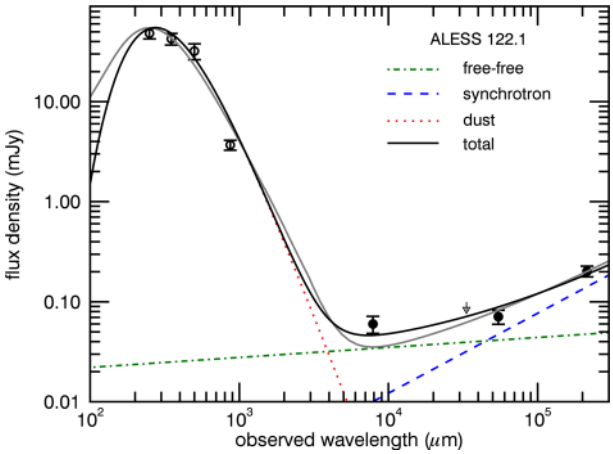

Figure 5. The FIR to radio SED of ALESS 122.1. We plot *Herschel* and ALMA FIR and submm data points (open circles), and the 1.4-GHz (Miller et al. 2013), 5.5-GHz (Huynh et al. 2015) and 38.1-GHz (this work) radio data (filled circle). The downward arrow denotes the 9.0-GHz 4σ limit (Huynh et al. in preparation). The thermal dust emission component with a temperature of 32 K is shown as a red dotted line. The radio free–free (green dot–dashed line) and synchrotron (blue dashed line) components are scaled to produce a best fit to the radio data (filled circles). The black solid line marks the total of all three components. For comparison, the best-fitting SED of Swinbank et al. (2014) is also shown (solid grey line).

Table 2. Radio SED fitting results for ALESS 122.1

$S_{38.1\,\rm GHz,\,total}$ (μJy)	$S_{38.1\,\rm GHz,\,ff}$ (μJy)	$S_{38.1\,\rm GHz,\,synch}$ (μJy)	$S_{38.1\,\rm GHz,\,dust}$ (μJy)
46 ± 14	34 ± 17	10 ± 3	2.7 (fixed)

contribution from dust, thermal free–free radio emission with a fixed slope of $\alpha = -0.1$ ($S \propto \nu^\alpha$), and a non-thermal synchrotron radio component with a fixed slope of $\alpha = -0.8$. The dust contribution is determined from a grey body SED ($S \propto B(\nu, T)\nu^\beta$), where $B(\nu, T)$ is the Planck blackbody and β is the emissivity index. We set the blackbody function to a temperature of 32 K, as determined by Swinbank et al. (2014) for ALESS 122.1, and adopt $\beta = 1.5$. The free–free and synchrotron radio components are then allowed to scale to fit the three radio continuum data points. The resulting best-fitting decomposition of the ALESS 122.1 SED, shown in Fig. 5, has a reduced χ^2 value of ∼2, indicating a reasonable fit.

The contributions to $S_{38.1\rm GHz}$ from dust, free–free and synchrotron radio emission are presented in Table 2. Using Condon (1992), we determine SFR ($M > 5\,$M$_\odot$) = 440 ± 220 M$_\odot$ yr^{-1} from the fitted radio free–free emission. Using an IMF similar to Kennicutt & Evans (2012), we account for stars with $1 < M < 5\,$M$_\odot$ using a Salpeter IMF and low-mass stars ($0.1 < M < 1\,$M$_\odot$) with a shallower Kroupa IMF, to find a radio free–free total SFR of 1400 ± 700 M$_\odot$ yr^{-1}. This is consistent with SFR of 940^{+60}_{-80} M$_\odot$ yr^{-1} derived from the infrared luminosity, showing that radio free–free emission has the potential to be a powerful measure of galaxy SFRs. The fitted thermal fraction of the radio emission from ALESS 122.1 is 73 ± 37, 47 ± 23 and 26 ± 13 per cent at 38.1, 5.5 and 1.4 GHz, respectively, i.e. 115, 16.6 and 4.2 GHz rest frame. This is consistent with the thermal fraction found in M82 (Condon 1992) and some $z < 0.5$ ULIRGs (Galvin et al. 2016). This result is from fitting to only three radio data points, and has a large uncertainty, but it shows the potential of radio free–free emission in measuring the SFRs of galaxies at these redshifts. A caveat

however is that an X-Ray stacking analysis by Wang et al. (2013) found that ALESS 122.1 is likely to contain an AGN. An additional flat spectrum AGN component cannot be ruled out with the current radio data.

Note that the same analysis cannot be performed on ALESS 67.1 because it does not have a 5.5 GHz detection.

5 CONCLUSIONS

We have presented the first results from an ATCA ^{12}CO(1–0) survey of cold molecular gas from ALMA-detected SMGs in the ECDFS.

In this first phase, we targeted two SMGS at $z \sim 2$. The main results from this work are as follows.

(i) We detect strong CO(1–0) emission from ALESS 122.1 and ALESS 67.1, which lie at $z = 2.0232$ and 2.1230, respectively. The CO line redshift is consistent with the optical spectroscopic redshift in both cases. The CO emission lines have FWHM $> 700\,\mathrm{km\,s^{-1}}$, which is as expected for more infrared-luminous SMGs. The CO(1–0) luminosities are $(13 \pm 2) \times 10^{10}$ and $(9.9 \pm 1.8) \times 10^{10}$ K km s^{-1} pc^2, which correspond to molecular gas masses of 13×10^{10} and 9.9×10^{10} M$_\odot$, for a conversion factor of $\alpha = 1.0$.

(ii) Assuming the CO(1–0) emitting region of ALESS 122.1 and ALESS 67.1 be constrained by the *HST* high-resolution optical counterpart, we use the optical source sizes (<0.5 arcsec, or 4.2 kpc at $z = 2$) and the measured CO linewidths to estimate dynamical masses of $M_{\rm dyn}\ \sin^2\ i \lesssim 5 \times 10^{11}$ M$_\odot$ for ALESS 122.1 and ALESS 67.1. The spatial offset between the redshifted and blueshifted components of the CO line gives a consistent dynamical mass of $M_{\rm dyn}\ \sin^2\ i = (2.1 \pm 1.1) \times 10^{11}$ M$_\odot$ and $(3.2 \pm 0.9) \times 10^{11}$ M$_\odot$ for ALESS 122.1 and ALESS 67.1, respectively, within 10–15 kpc. These dynamical masses are similar to the median dynamical masses of typical SMGs (Bothwell et al. 2013).

The stellar masses were combined with the gas mass to derive total baryonic masses of $(1.9 \pm 1.1) \times 10^{11}$ M$_\odot$ and $(1.4 \pm 0.9) \times 10^{11}$ M$_\odot$ for ALESS 122.1 and ALESS 67.1, respectively. This implies a gas mass fraction greater than 70 per cent.

(iii) We examine the SF efficiency of SMGs, using the observed $L_{\rm FIR}$ and $L'_{\rm CO(1-0)}$ luminosities. We find that ULIRGs and SMGs have a similar slope in $L_{\rm FIR}$ versus $L'_{\rm CO(1-0)}$. Together the ULIRG and SMG populations show a slope of 0.60 ± 0.08, while LIRGs and BzKs show a slightly steeper relation with slope $= 0.86 \pm 0.08$. A larger sample with more high-redshift CO(1–0) detections is required to definitely conclude that there is a difference in the slope for these populations, but this is some evidence that there is a difference in the SF modes of LIRGS and BzKs versus more extreme ULIRGs and SMGs.

(iv) We derive gas-to-dust ratios $\delta_{\rm GDR} = 170 \pm 30$ and $\delta_{\rm GDR} = 140 \pm 30$ for ALESS 122.1 and ALESS 67.1, respectively. ALESS 122.1 appears to have an unusually large gas-to-dust ratio, due to its large inferred gas reservoir. We convert the ALMA submm continuum flux densities to luminosities and find monochromatic 850-μm luminosity-to-mass ratios, $L_{850}/M_{\rm gas}$, of $(0.75 \pm 0.11) \times 10^{20}$ and $(1.3 \pm 0.3) \times 10^{20}$ erg s^{-1} Hz^{-1} M$_\odot^{-1}$ for ALESS 122.1 and ALESS 67.1, respectively, using our measured CO molecular gas masses.

(v) The 38.1 GHz continuum detection of ALESS 122.1 was combined with literature radio data at 1.4 and 5.5 GHz to estimate the free–free radio emission. We find that free–free emission makes up 73 ± 37 per cent of the radio emission at 38.1 GHz (115 GHz rest frame). Converting the free–free emission to SFR yields an SFR of 1400 ± 700 M$_\odot$ yr^{-1}, consistent with the SFR derived from total infrared luminosity. An AGN contribution to the radio emission cannot be ruled out, however. Further sensitive high-frequency radio observations between 10 and 100 GHz (rest frame) would provide better constraints on free–free radio emission.

CO(1–0) detections are important as the $J = 1$ transition removes uncertainties in the estimated line luminosities introduced by excitation conditions of the molecular gas. Our work has no biases from high-J CO transitions, which has hampered earlier work, and illustrates the importance of ATCA observations at these frequencies (7-mm band, 30–50 GHz).

The remaining SMGs in the ALESS sample will be targeted with ATCA in the near future as part of our ongoing survey of CO(1–0) from SMGs at $z \sim 2$. The ALESS sample of SMGs is also being followed up with ALMA for higher J CO lines and other molecular line tracers of gas such as [C II] and [N II]. The combination of the $J = 1$ transition CO observations from ATCA with the ALMA observations will reveal the gas excitation conditions and other properties, such as metallicity, in SMGs, shedding even more light on the physical conditions of molecular gas in high-redshift galaxies.

ACKNOWLEDGEMENTS

The Australia Telescope Compact Array is part of the Australia Telescope National Facility, which is funded by the Australian Government for operation as a National Facility managed by CSIRO. IRS acknowledges support from the STFC (ST/L00075X/1), the ERC Advanced Investigator Programme DUSTYGAL (321334) and a Royal Society Wolfson Merit Award. HD acknowledges financial support from the Spanish Ministry of Economy and Competitiveness (MINECO) under the 2014 Ramón y Cajal programme MINECO RYC-2014-15686. CMC thanks the College of Natural Sciences at the University of Texas at Austin. BE acknowledges funding from the European Union 7th Framework Programme (FP7-PEOPLE-2013-IEF) under REA grant 624351. RJI acknowledges support from ERC Advanced Grant 321302, COSMICISM. JLW is supported by a European Union COFUND/Durham Junior Research Fellowship under EU grant agreement number 267209 and acknowledges additional support from STFC (ST/L00075X/1). WNB acknowledges support from STScI grant HST-GO-12866.01-A.

REFERENCES

Aravena M. et al., 2010, ApJ, 718, 177
Aravena M. et al., 2012, MNRAS, 426, 258
Blain A. W., Smail I., Ivison R. J., Kneib J.-P., Frayer D. T., 2002, Phys. Rep., 369, 111
Bothwell M. S. et al., 2010, MNRAS, 405, 219
Bothwell M. S. et al., 2013, MNRAS, 429, 3047
Carilli C. L., Walter F., 2013, ARA&A, 51, 105
Carilli C. L. et al., 2010, ApJ, 714, 1407
Casey C. M. et al., 2012, ApJ, 761, 140
Casey C. M., Narayanan D., Cooray A., 2014, Phys. Rep., 541, 45
Chapman S. C., Blain A. W., Smail I., Ivison R. J., 2005, ApJ, 622, 772
Chary R., Elbaz D., 2001, ApJ, 556, 562
Chen C.-C. et al., 2015, ApJ, 799, 194
Chung A., Narayanan G., Yun M. S., Heyer M., Erickson N. R., 2009, AJ, 138, 858
Condon J. J., 1992, ARA&A, 30, 575
Coppin K. E. K. et al., 2010, MNRAS, 407, L103
Daddi E. et al., 2010, ApJ, 713, 686
Damen M. et al., 2011, ApJ, 727, 1
Danielson A. L. R. et al., 2011, MNRAS, 410, 1687

Danielson A. L. R. et al., 2016, in press
Davé R., Finlator K., Oppenheimer B. D., Fardal M., Katz N., Kereš D., Weinberg D. H., 2010, MNRAS, 404, 1355
Downes D., Solomon P. M., 1998, ApJ, 507, 615
Draine B. T. et al., 2007, ApJ, 663, 866
Eales S. et al., 2010, PASP, 122, 499
Eales S. et al., 2012, ApJ, 761, 168
Emonts B. H. C. et al., 2011, MNRAS, 415, 655
Emonts B. H. C. et al., 2014, MNRAS, 438, 2898
Emonts B. H. C. et al., 2015, MNRAS, 451, 1025
Engel H. et al., 2010, ApJ, 724, 233
Galvin T. J., Seymour N., Filipović M. D., Tothill N. F. H., Marvil J., Drouart G., Symeonidis M., Huynh M. T., 2016, MNRAS, 461, 825
Geach J. E. et al., 2017, MNRAS, 465, 1789
Genzel R. et al., 2010, MNRAS, 407, 2091
Gooch R., 1996, in Jacoby G. H., Barnes J., eds, ASP Conf. Ser. Vol. 101, Astronomical Data Analysis Software and Systems V. Astron. Soc. Pac., San Francisco, p. 80
Greve T. R., Ivison R. J., Papadopoulos P. P., 2003, ApJ, 599, 839
Greve T. R. et al., 2005, MNRAS, 359, 1165
Gruppioni C. et al., 2013, MNRAS, 432, 23
Haarsma D. B., Partridge R. B., Windhorst R. A., Richards E. A., 2000, ApJ, 544, 641
Hainline L. J., Blain A. W., Smail I., Alexander D. M., Armus L., Chapman S. C., Ivison R. J., 2011, ApJ, 740, 96
Harris A. I. et al., 2012, ApJ, 752, 152
Hayward C. C., Narayanan D., Kereš D., Jonsson P., Hopkins P. F., Cox T. J., Hernquist L., 2013, MNRAS, 428, 2529
Helou G., Khan I. R., Malek L., Boehmer L., 1988, ApJS, 68, 151
Hildebrand R. H., 1983, QJRAS, 24, 267
Hodge J. A. et al., 2013, ApJ, 768, 91
Hopkins A. M., Beacom J. F., 2006, ApJ, 651, 142
Hopkins P. F., Hernquist L., 2010, MNRAS, 402, 985
Huynh M. T. et al., 2014, MNRAS, 443, L54
Huynh M. T., Bell M. E., Hopkins A. M., Norris R. P., Seymour N., 2015, MNRAS, 454, 952
Ivison R. J., Papadopoulos P. P., Smail I., Greve T. R., Thomson A. P., Xilouris E. M., Chapman S. C., 2011, MNRAS, 412, 1913
Jenkins E., 2004, in McWilliam A., Rauch M., eds, Origin and Evolution of the Elements. Cambridge Univ. Press, Cambridge
Kennicutt R. C., Evans N. J., 2012, ARA&A, 50, 531
Kennicutt R. C. Jr., 1989, ApJ, 344, 685
Kennicutt R. C. Jr., 1998, ApJ, 498, 541
Lilly S. J., Eales S. A., Gear W. K. P., Hammer F., Le Fèvre O., Crampton D., Bond J. R., Dunne L., 1999, ApJ, 518, 641
Madau P., Dickinson M., 2014, ARA&A, 52, 415
Magnelli B. et al., 2012, A&A, 539, A155
Magnelli B. et al., 2013, A&A, 553, A132
Middelberg E., Sault R. J., Kesteven M. J., 2006, PASA, 23, 147
Miller N. A. et al., 2013, ApJS, 205, 13
Narayanan D. et al., 2015, Nature, 525, 496
Papadopoulos P. P., Allen M. L., 2000, ApJ, 537, 631
Papadopoulos P., Ivison R., Carilli C., Lewis G., 2001, Nature, 409, 58
Papadopoulos P. P., van der Werf P. P., Xilouris E. M., Isaak K. G., Gao Y., Mühle S., 2012, MNRAS, 426, 2601
Rix H.-W. et al., 2004, ApJS, 152, 163
Saintonge A. et al., 2012, ApJ, 758, 73
Sault R. J., Killeen N. E. B., 1999, MIRIAD User's Guide. Australia Telescope National Facility, Sydney, Australia
Schmidt M., 1959, ApJ, 129, 243
Scoville N. et al., 2014, ApJ, 783, 84
Seymour N. et al., 2008, MNRAS, 386, 1695
Simpson J. M. et al., 2014, ApJ, 788, 125
Smolčić V. et al., 2012, A&A, 548, A4
Solomon P. M., Vanden Bout P. A., 2005, ARA&A, 43, 677
Solomon P. M., Downes D., Radford S. J. E., Barrett J. W., 1997, ApJ, 478, 144
Swinbank A. M. et al., 2011, ApJ, 742, 11
Swinbank A. M. et al., 2014, MNRAS, 438, 1267
Tacconi L. J. et al., 2010, Nature, 463, 781
Valiante E. et al., 2016, MNRAS, 462, 3146
Wang S. X. et al., 2013, ApJ, 778, 179
Wardlow J. L. et al., 2011, MNRAS, 415, 1479
Weiß A. et al., 2009, ApJ, 707, 1201
Williams M. J., Bureau M., Cappellari M., 2010, MNRAS, 409, 1330
Wilson W. E. et al., 2011, MNRAS, 416, 832

[1]*International Centre for Radio Astronomy Research, M468, University of Western Australia, Crawley, WA 6009, Australia*
[2]*CSIRO Astronomy and Space Science, 26 Dick Perry Avenue, Kensington, WA 6151, Australia*
[3]*Centro de Astrobiología (INTA-CSIC), Ctra de Torrejón a Ajalvir, km 4, E-28850 Torrejón de Ardoz, Madrid, Spain*
[4]*CSIRO Astronomy and Space Science, PO Box 76, Epping, NSW 1710, Australia*
[5]*National Radio Astronomy Observatory, 1003 Lopezville Rd, Socorro, NM 87801, USA*
[6]*International Centre for Radio Astronomy Research, Curtin University, Bentley, WA 6102, Australia*
[7]*Centre for Extragalactic Astronomy, Department of Physics, Durham University, South Road, Durham DH1 3LE, UK*
[8]*Department of Astronomy and Astrophysics, 525 Davey Lab, The Pennsylvania State University, University Park, PA 16802, USA*
[9]*Institute for Gravitation and the Cosmos, The Pennsylvania State University, University Park, PA 16802, USA*
[10]*Department of Physics, The Pennsylvania State University, University Park, PA 16802, USA*
[11]*Department of Astronomy, the University of Texas at Austin, 2515 Speedway Blvd, Stop C1400, Austin, TX 78712, USA*
[12]*Dalhousie University, Halifax, NS B3H 3J5, Canada*
[13]*Instituto de Astrofísica de Canarias (IAC), E-38205 La Laguna, Tenerife, Spain*
[14]*Universidad de La Laguna, Dpto. Astrofísica, E-38206 La Laguna, Tenerife, Spain*
[15]*Institut für Astronomie, Universität Wien, Türkenschanzstrasse 17, A-1160 Wien, Austria*
[16]*Leiden Observatory, Leiden University, PO Box 9513, NL-2300 RA Leiden, the Netherlands*
[17]*European Southern Observatory, Karl-Schwarzschild-Str. 2, D-85748 Garching bei München, Germany*
[18]*Institute for Astronomy, University of Edinburgh, Royal Observatory, Blackford Hill, Edinburgh EH9 3HJ, UK*
[19]*Max-Planck-Institut für Astronomie, Königstuhl 17, D-69117 Heidelberg, Germany*

This paper has been typeset from a TEX/LATEX file prepared by the author.